Supplementary information: Long-range magnetic order with disordered spin orientations in a high-entropy antiferromagnet

(Dated: February 24, 2026)

CONTENTS

SUPPLEMENTARY NOTE 1. TRANSFORMATION BETWEEN HEXAGONAL AND MONOCLINIC NOTATIONS

$HEPS_3$ adopts a monoclinic crystal structure with a slightly distorted honeycomb lattice (Fig. S1). While the monoclinic notation is used throughout the main text, it is essential to clarify its relationship to the hexagonal unit cell notation — the latter typically used for non-distorted honeycomb lattices. Figure S2 illustrates the transformation between monoclinic and hexagonal notations in both real and reciprocal space. The 3D magnetic peak $\mathbf{Q} = (0, 1, 0)$ (zone center) in monoclinic notation corresponds to $\mathbf{Q} = (-1/2, 1/2, 0)$ (zone boundary) in hexagonal notation.

SUPPLEMENTARY NOTE 2. MORE SAMPLE CHARACTERIZATION

To confirm the reproducibility of the phase transitions, we repeat the magnetic susceptibility measurements on several $HEPS_3$ single crystals, obtaining consistent results (Fig. S3). Above 80 K, the magnetic susceptibility follows

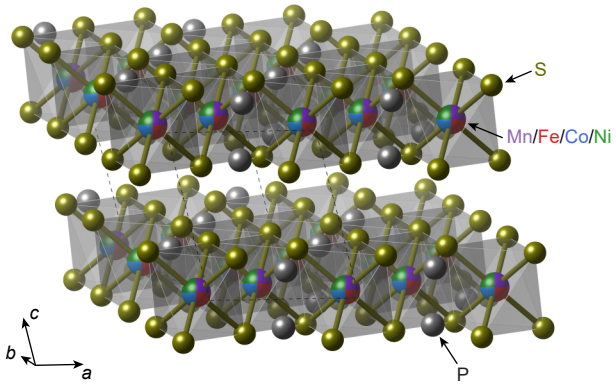

FIG. S1. **Lattice structure of $HEPS_3$.**

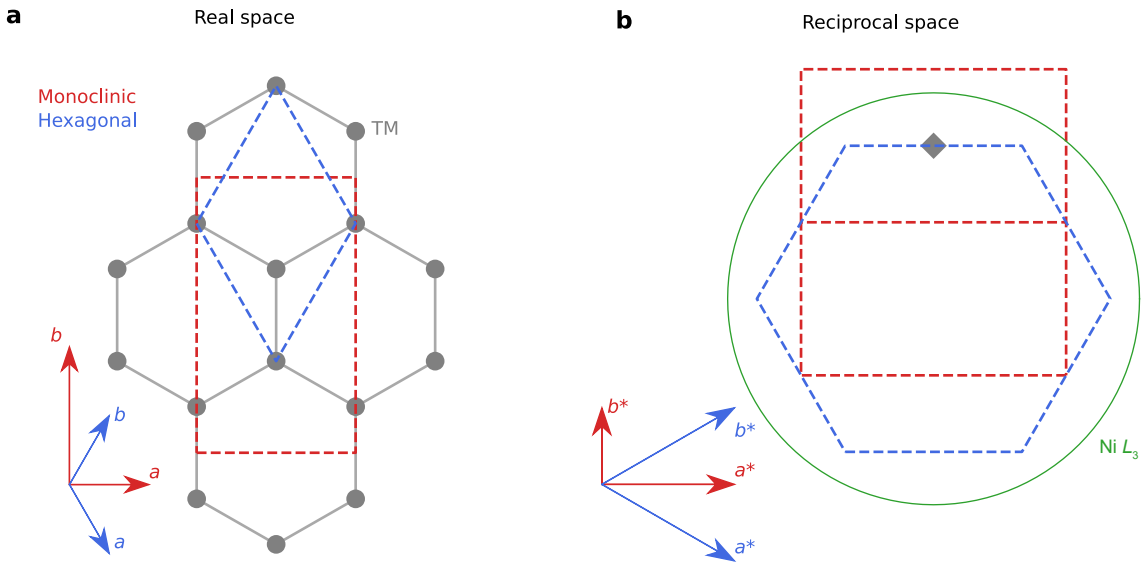

FIG. S2. **Schematics illustrating hexagonal and monoclinic unit cells. a,** Sketch of the real space of a honeycomb lattice. The dashed lines indicate the unit cells for the hexagonal and monoclinic lattices. **b,** Reciprocal space projected onto the *ab* plane. The dashed lines outline the Brillouin zones for the hexagonal and monoclinic notations. The diamond marker denotes a 3D magnetic peak. The green circle illustrates the reciprocal space that can be accessed by Ni L_3-edge RSXS. TM, transition metal.

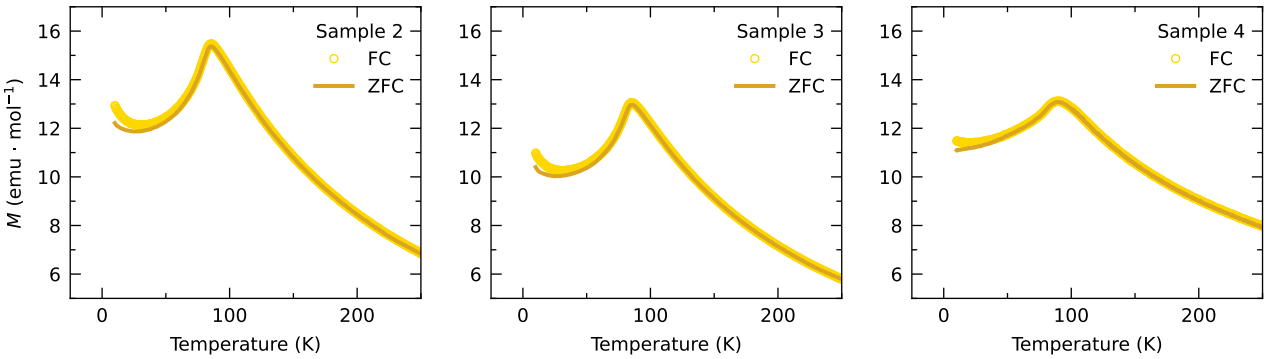

FIG. S3. **Magnetic susceptibility measurements of multiple different $HEPS_3$ single crystals.**

Curie-Weiss behavior (Fig. S4), with a Curie-Weiss temperature of -43 K and a Curie constant of 1.147 emu·K/mol. This corresponds to an effective moment of 3.03 μ_B/site, implying a saturated moment of 2.19 μ_B/site assuming a g-factor of 2. This value is slightly higher than that derived from neutron diffraction measurements.

Our neutron diffraction and resonant soft x-ray scattering (RSXS) measurements unambiguously demonstrate that the transition at 72 K originates from the long-range magnetic order. By contrast, the nature of the 40 K transition remains uncertain, but we can formulate some tentative expectations. Below 40 K, the zero-field-cooling (ZFC) and field-cooling (FC) curves split, indicating spin-glass behaviors or spin reorientations. However, magnetic susceptibility and neutron diffraction (as well RSXS) probe the magnetic responses on different length and time scales. Thus, it is possible that the process corresponding to the 40 K transition happens on scales beyond the momentum and temporal resolution of conventional neutron and x-ray scattering techniques, making the investigation of this transition fall beyond the scope of the present work.

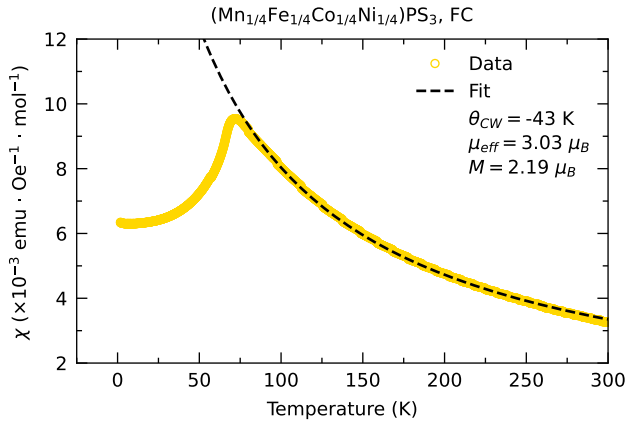

FIG. S4. **Curie-Weiss fit of the magnetic susceptibility above 80 K.**

SUPPLEMENTARY NOTE 3. STRUCTURAL DISORDER

Here we examine structural disorder in $HEPS_3$, particularly stacking faults within its layered architecture. In an ideal $TMPX_3$ structure, honeycomb layers exhibit perfect A-B-C stacking along the out-of-plane direction. However, local deviations such as A-A or A-B-A-B stacking can occur, leading to stacking fault disorder that manifests as diffuse scattering along the L direction in diffraction patterns. Figure S5a&b present the neutron diffraction and x-ray diffraction (XRD) patterns in the $0KL$ plane. While structural reflections satisfying $H + K = 6n$, where n is an integer, exhibit no indication of diffuse scattering, diffusive signals appear along L for $\mathbf{Q} = (0, -4, L)$ and $\mathbf{Q} = (0, -2, L)$, a hallmark of stacking faults. This can be seen more clearly in the L cuts presented in Fig. S5c&d. Note that stacking fault effects cancel out for $H + K = 6n$ reflections [1]. Additionally, the honeycomb lattice symmetry naturally gives rise to three equivalent structural domains [2]. In our neutron diffraction data collected from a large single crystal (several millimeters in size), this multidomain configuration produces nuclear signals at non-integer L positions (Fig. S5c). Conversely, XRD measurements performed on a smaller crystal ($\approx 100\mu$m) using a laboratory diffractometer revealed single-domain characteristics, as indicated by the absence of non-integer L signals (Fig. S5d). Notably, the magnetic diffuse scattering exhibits slightly broader features compared to the stacking-fault-induced nuclear diffuse signals (Fig. S5c), suggesting contributions from other sources for the two-dimensional (2D) magnetic signals, such as reduced out-of-plane magnetic correlations.

SUPPLEMENTARY NOTE 4. REFINEMENT OF THE NEUTRON DIFFRACTION DATA

For $HEPS_3$, when transitioning from the high-symmetry hexagonal notation to the lower-symmetry monoclinic notation, the system generates three equivalent domains, each oriented at 120° intervals relative to one another via rotations about the c^*-axis [2]. In the neutron diffraction data, peaks from all three monoclinic domains were observed, as evident from the six-fold magnetic peaks shown in Fig. 2b of the main text. We integrated the peaks from the most populated monoclinic domain and refined the structures via Fullprof software [3]. It was noticed that nuclear peaks with indices satisfying the condition $3H \pm K = 6n$, where n is an integer, are overlapped by all three domains. Two different protocols were implemented: (1) excluding them from the refinement or (2) accounting for their intensities as contributions from all three domains. Both approaches yielded essentially identical refinement results.

Figure S6a shows the refinement of the nuclear peaks at 6 K. With the overlapped peaks included in the refinement, we achieved agreement factors of $R_F = 3.78$ and $R_{F^2} = 7.35$. The refinement results support the conclusion that Mn, Fe, Co, and Ni are randomly distributed on the same site with a 25% occupancy for each.

For the magnetic peaks, there are no peak-overlapping issues as peaks from different domains are well separated in the reciprocal space. For the refinement, we integrated the sharp intensity regions of the 3D magnetic signals. The data can be well refined using a zigzag magnetic structure with moments confined to the ac^* plane, resulting in agreement factors of R_F=4.49 and R_{F^2}=8.37 (Fig S6b). During the refinement, we examined form factors of Mn^{2+}, Fe^{2+}, Co^{2+}, and Ni^{2+}, respectively, and the resulting parameters showed no significant differences. Employing the Fe^{2+} form factor, the refined magnetic moment exhibits components of 1.14(1) μ_B along the c^*-axis and -0.99(1) μ_B along the a-axis. This yields a total magnetic moment of 1.51(1) μ_B tilted 49° away from the honeycomb plane.

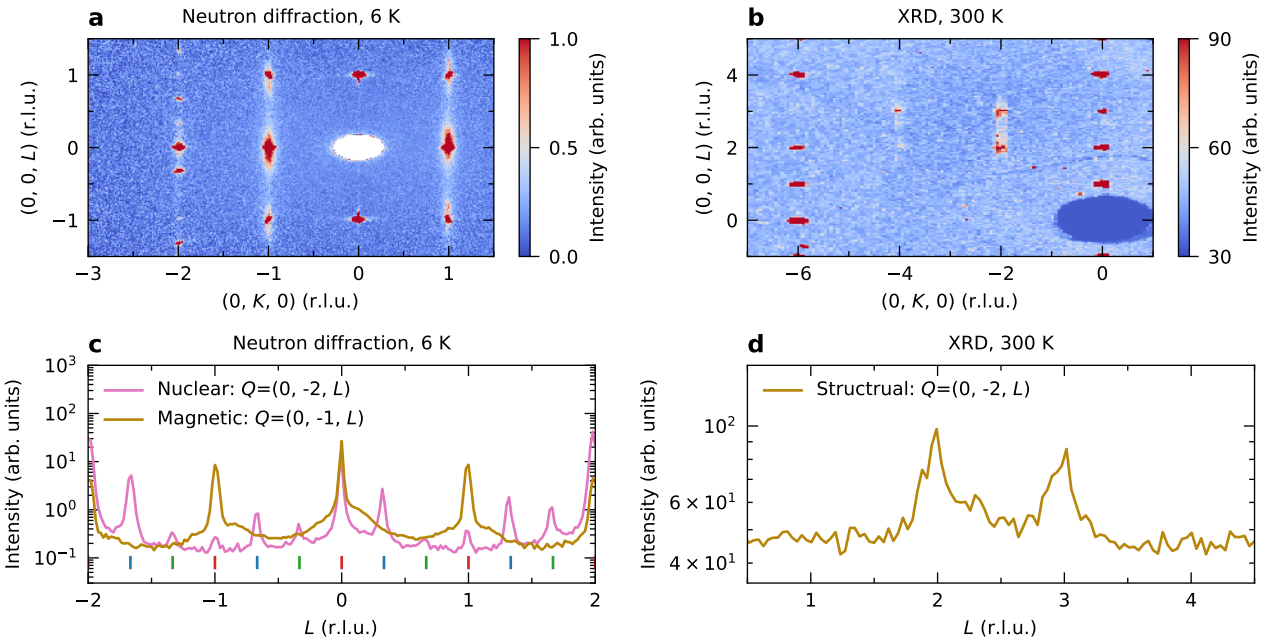

FIG. S5. **Stacking fault characterization in $HEPS_3$. a, b,** Neutron diffraction and XRD patterns in the $0KL$ plane, respectively. Magnetic signals appear at $\mathbf{Q} = (0, \pm 1, L)$, while all other reflections correspond to nuclear (structural) contributions. **c, d,** One-dimensional $\mathbf{Q}$ cuts along the L direction. The blue, red, and green vertical ticks denote nuclear reflections originating from three distinct crystallographic domains.

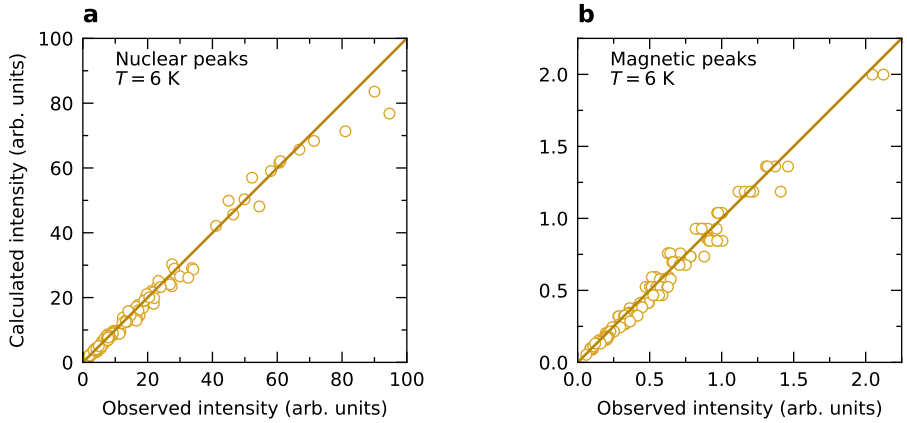

FIG. S6. **Refinement of neutron diffraction data.** Comparison between measured and calculated intensities for **a,** nuclear peaks, and **b,** 3D magnetic signals. The latter are simulated based on a zigzag magnetic structure as discussed in the text.

SUPPLEMENTARY NOTE 5. SINGLE-ION ANISOTROPY

Single-ion anisotropy arises from the combined effects of electronic filling, crystal electric field (CEF) splitting, and spin-orbit coupling (SOC). Here, supplemented with exact diagonalization (ED) calculations of atomic models, we demonstrate how these parameters, particularly electronic filling and trigonal distortion, influence the single-ion anisotropy.

For a TMO_6 octahedron, the cubic CEF splits the ten $3d$ orbitals into a high-energy e_g manifold and a low-energy t_{2g} manifold, separated by an energy difference of $10D_q$. Trigonal distortion, which is relevant for $HEPS_3$, further splits the t_{2g} states while leaving the e_g manifold unaffected. Since the TMO_6 octahedra in $HEPS_3$ are elongated, the corresponding trigonal field is positive ($\delta > 0$), splitting the t_{2g} manifold into a low-energy singlet and a high-energy doublet. In contrast, the neighboring magnetic cations induce a negative trigonal field ($\delta < 0$) [4]. Based on the single-ion anisotropy observed in $TMPX_3$, we conclude that in $HEPS_3$, the overall trigonal field is negative. Here,

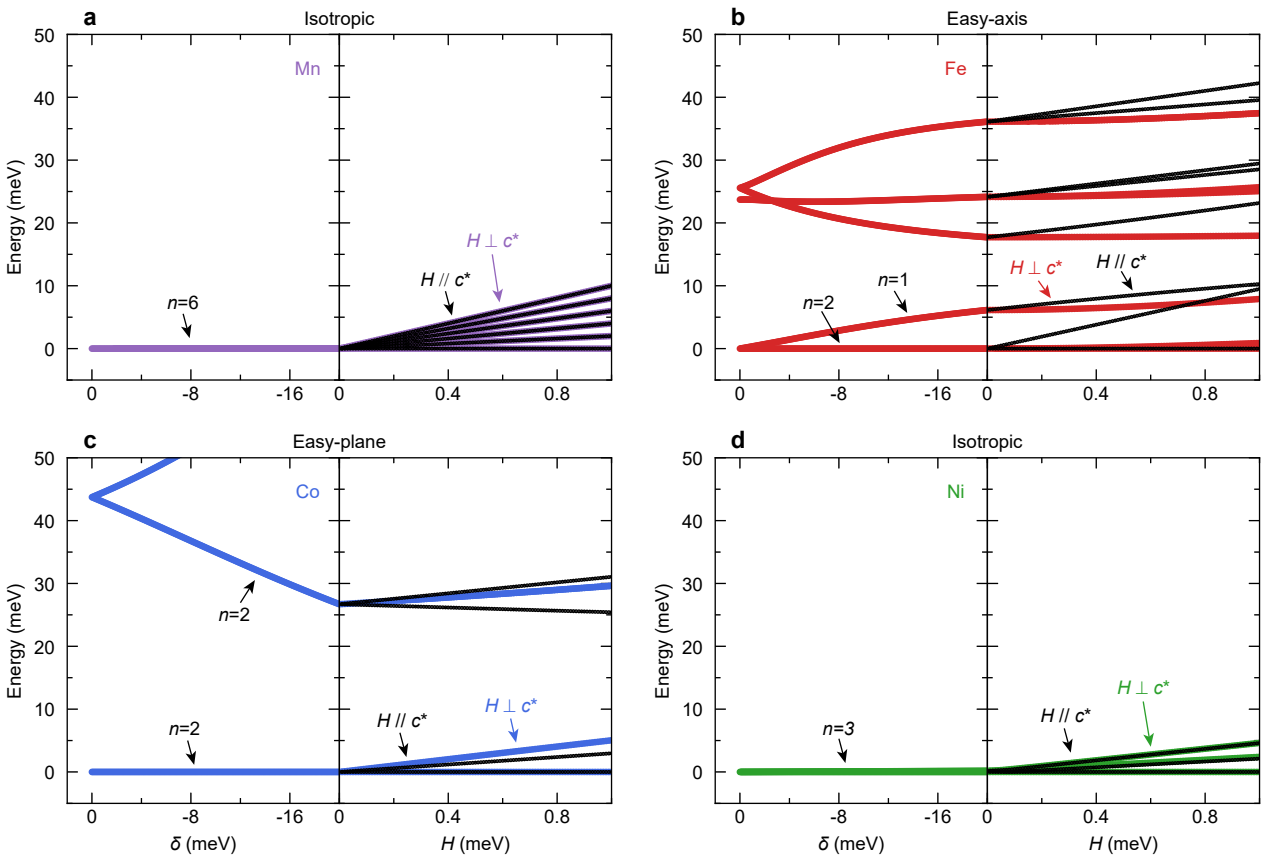

FIG. S7. **Exact diagonalization calculations of atomic models. a,** Left panel: energy level diagram for a Mn^{2+} (d^5) ion as a function of trigonal distortion δ. Here, the cubic crystal field splitting $10D_q$ is fixed to 1 eV, and the spin-orbit coupling is fixed to the atomic value. Note that n is the degree of degeneracy. Right panel: Zeeman splitting as a function of external magnetic fields applied parallel and perpendicular to the $\mathbf{c}^*$ direction, respectively, with trigonal distortion $\delta = -20$ meV. **b-d,** Same as **a** but for Fe^{2+} (d^6), Co^{2+} (d^7), and Ni^{2+} (d^8), respectively.

only the orbital degree of freedom is considered. Incorporating SOC, which is weak but finite for $3d$ elements, further reduces the symmetry.

We now focus on the ED calculations, performed using an atomic model that includes all ten spin-resolved $3d$ orbitals. The Hund's coupling is set to 1 eV, and the cubic CEF splitting is fixed at $10D_q = 1$ eV. The SOC strength is varied according to the atomic values of the respective ions. For the Mn^{2+} ion ($3d^5$) in the high-spin state, the half-filled $3d$ shell leads to a ground state with $S = 5/2$ ($n = 6$, n is the degeneracy degree) and quenched orbital momentum, rendering it insensitive to trigonal distortion (Fig. S7a). The ground state exhibits isotropic Zeeman splitting under magnetic fields applied along different directions, indicating negligible single-ion anisotropy.

For the Fe^{2+} ion ($3d^6$), in the absence of trigonal distortion, the combination of cubic CEF and SOC yields a triplet ground state ($n = 3$) and a nearly degenerate quintuplet excited state ($n = 5$). Note that finite SOC breaks down the $S = 2$ state here. Applying trigonal distortion, the triplet ground state splits into a singlet and a doublet (Fig. S7b). If exchange interactions are sufficiently strong, these states recombine into a triplet, and the intrinsic energy gap can be mapped into the single-ion anisotropy. Upon applying a magnetic field, the energy change is more pronounced along the $\mathbf{c}^*$ direction, indicating easy-axis anisotropy, consistent with the spin orientation observed in $FePS_3$.

In contrast, since SOC plays a more important role for Co^{2+} ion ($3d^7$), its ground state is a well-defined doublet, which remains robust with trigonal distortion but develops distinct anisotropy (Fig. S7c). The Zeeman splitting is less pronounced when the magnetic field is applied along the $\mathbf{c}^*$ direction, indicating easy-plane anisotropy, in line with the spin orientation observed in $CoPS_3$. Notably, with the same trigonal distortion, Fe^{2+} exhibits easy-axis anisotropy, whereas Co^{2+} prefers easy-plane anisotropy due to their distinct electronic filling.

Similar to Mn^{2+}, the Ni^{2+} ion ($3d^8$) with a half-filled e_g manifold exhibits quenched orbital degrees of freedom, leading to a triplet ground state, which is inert to trigonal distortion and shows isotropic Zeeman splitting (Fig. S7d).

It is worth noting that thus far, we have only considered high-energy parameters, such as cubic CEF, SOC, and

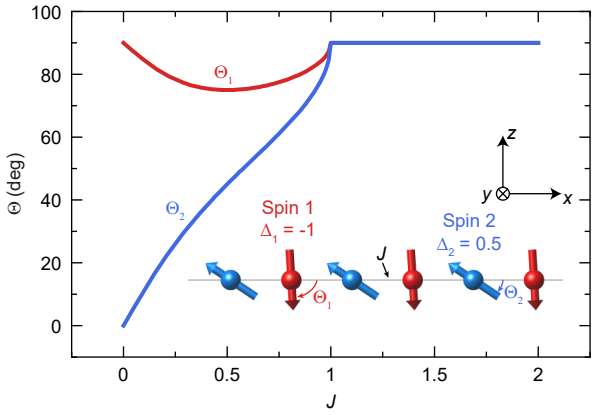

FIG. S8. **Calculated exchange interaction dependent spin orientations.** We adopt an antiferromagnetic spin chain composed of two types of atoms arranged alternatively, with distinct single-ion anisotropies. The spin orientations are then determined by tuning the intra-chain exchange interaction J.

the trigonal field. These parameters cause Fe^{2+} and Co^{2+} ions to exhibit robust single-ion anisotropy, whereas Mn^{2+} and Ni^{2+} ions behave nearly isotropic. Other low-energy parameters, such as lattice distortion beyond the trigonal field, can introduce further anisotropy and determine the spin orientation for Mn^{2+} and Ni^{2+}. Order-by-disorder and anisotropic exchange interactions, such as Kitaev terms, may also play a role [5]. Nevertheless, we can conclude that the spin orientations for Fe^{2+} and Co^{2+} ions are more resistant to competition with exchange interactions due to their substantial single-ion anisotropy.

Furthermore, we would like to emphasize that the determined spin orientation for each element is an average effect. For ions of the same element, local distortion varies from site to site due to atomic disorder intrinsic to high-entropy materials. As an example, the detailed CEF for Mn^{2+} ions depends on whether neighboring ions are Mn^{2+}, Fe^{2+}, Co^{2+}, or Ni^{2+}. Consequently, single-ion anisotropies may vary across the lattice for each element. Nonetheless, the variation is subtle, and our data unambiguously demonstrate that the average spin orientations for different elements are distinct.

SUPPLEMENTARY NOTE 6. COMPETITION BETWEEN SINGLE-ION ANISOTROPY AND EXCHANGE INTERACTIONS

To demonstrate the competition between single-ion anisotropy and exchange interactions, we construct a toy model: an antiferromagnetic spin chain composed of two types of atoms arranged alternatively, labeled as Spin 1 and Spin 2. We adopt the Hamiltonian:

$$\mathcal{H} = J\sum_{\langle ij\rangle} S_i S_j + \Delta_1 \sum_i (S_1^z)^2 + \Delta_2 \sum_j (S_2^z)^2 \tag{1}$$

where J is the intra-chain exchange interaction, $\langle ij\rangle$ denotes bond sums along the chain, and Δ_1 and Δ_2 are single-ion anisotropies for Spin 1 and Spin 2, respectively. To reflect the co-existence and competition of easy-plane and easy-axis anisotropies in $HEPS_3$, here, spin 1 is set to present strong easy-axis anisotropy ($\Delta_1 = -1$) and Spin 2 intermediate easy-plane anisotropy ($\Delta_2 = 1/2$). The Hamiltonian is solved within the mean-field framework. When $J = 0$, Spin 1 and Spin 2 align along the z and x directions, respectively, following their single-ion anisotropy (Fig. S8). We define Θ as the angle between the spin and the x direction, following the definition in the main text. Thus, $\Theta_1 = 90°$ for Spin 1 and $\Theta_2 = 0°$ for Spin 2.

When J is non-zero, it favors antiparallel alignment for the Spin 1 and Spin 2 sublattices, which competes with the single-ion anisotropy. Consequently, Spin 1 starts to rotate toward the x axis ($\Theta_1 < 90°$) and Spin 2 rotates toward the z axis ($\Theta_2 > 0°$). As Δ_1 is larger than Δ_2, Θ_1 is more robust than Θ_2.

When J is sufficiently large, it enforces an antiparallel alignment for both Spin 1 and Spin 2, making them aligned along the z direction due to the stronger single-ion anisotropy of Spin 1.

The situation is much more complex in real materials. There are multiple types of exchange interactions and single-ion anisotropies, making effective modeling difficult. Nevertheless, our toy model here qualitatively demonstrates that

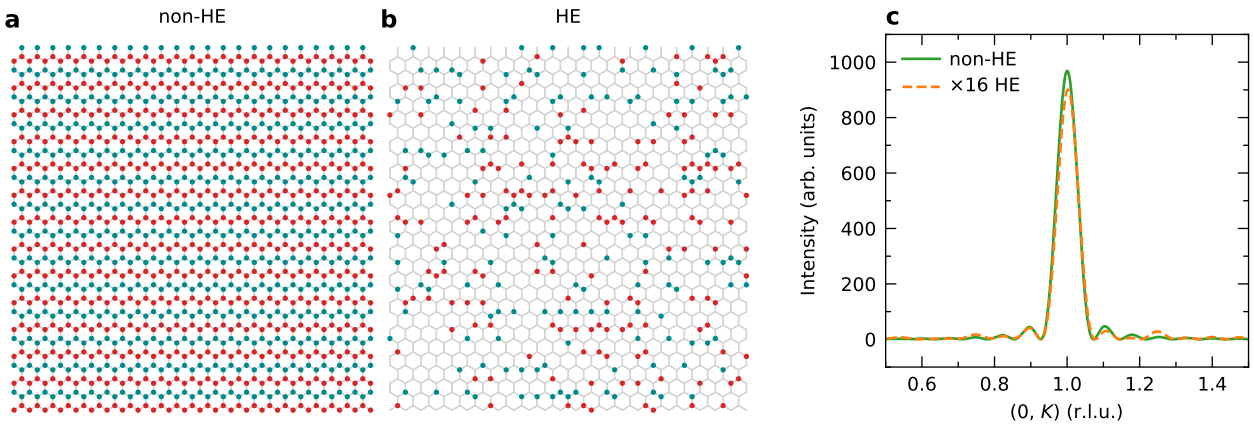

FIG. S9. **Simulation of the structure factor of $HEPS_3$. a, b,** Honeycomb lattice for the non-HE and HE scenarios, respectively. For the HE case, only a quarter of the sites are retained randomly. The red and blue dots indicate the spin-up and spin-down sites, respectively. **c,** Calculated squared magnetic structure factor across the magnetic peak of zigzag magnetic order.

the competition between single-ion anisotropy and exchange interactions can indeed trigger the element-specific spin orientations illustrated in the main text.

SUPPLEMENTARY NOTE 7. STRUCTURE FACTOR SIMULATION

To better understand the magnetic signals observed via RSXS, we developed a simple toy model to simulate the magnetic order in $HEPS_3$. Consider a 2D honeycomb lattice where each site is occupied by a single type of magnetic atom (Fig. S9a). A zigzag spin arrangement results in a magnetic peak at $\mathbf{Q}= (0, 1)$, which is also the propagation vector (Fig. S9c). To mimic the HE scenario in $HEPS_3$, we randomly remove three-quarters of the atoms while maintaining the zigzag spin arrangement (Fig. S9b). Interestingly, the magnetic signals at $\mathbf{Q}= (0, 1)$ persist, with the same peak width determined by the system size. However, the peak amplitude was reduced by a factor of 16, as only a quarter of the atoms contribute to the magnetic signals (Fig. S9c). In real materials, the situation becomes more complex. To stabilize long-range magnetic order, it is necessary to account for exchange interactions, which play a crucial role in determining the magnetic structure.

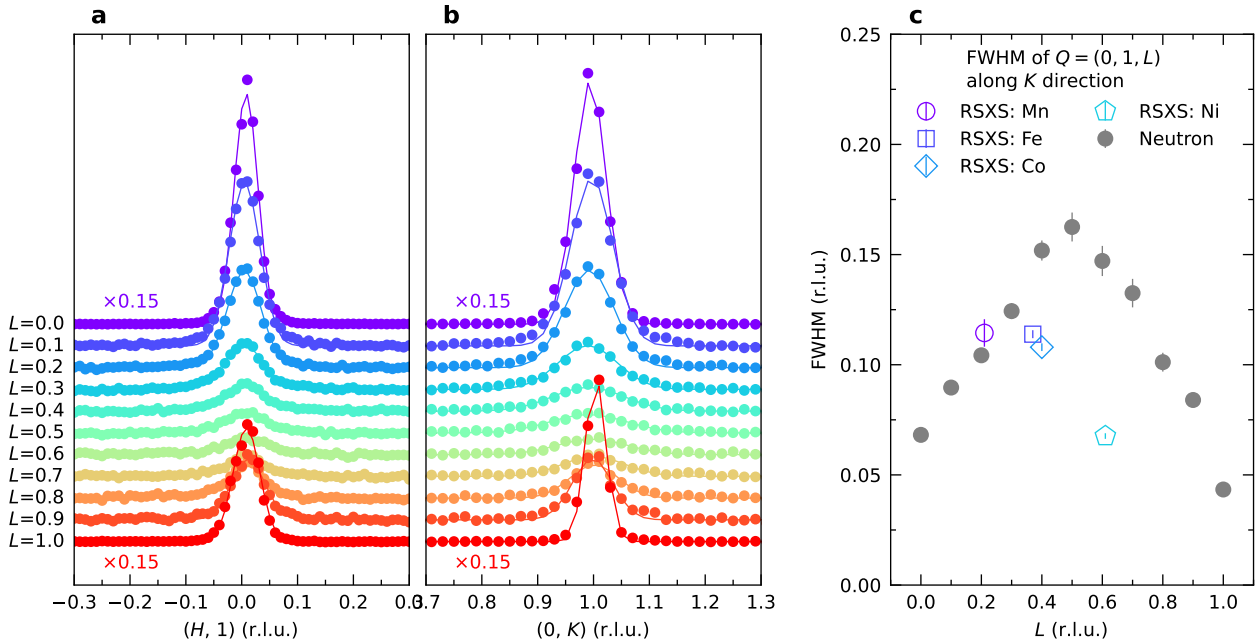

FIG. S10. **Magnetic peak widths obtained from neutron diffraction and RSXS. a,** One-dimensional **Q** cuts along H direction across $\mathbf{Q} = (0, 1, L)$ with various L. The dots represent neutron diffraction data, and the solid lines are fits with Gaussian profiles. **b, Q** cuts along K direction. **c,** L dependent peak widths obtained from fitting. In the neutron diffraction data, the 2D magnetic peak width decreases when approaching the 3D signals at $L = 0$ and $L = 1$. This behavior is not observed in RSXS data since RSXS probes element-specific magnetic correlations. Furthermore, the **Q** resolution in RSXS varies across different elements due to differences in incident energy, penetration depth, and beam footprint, complicating direct comparisons of peak widths between elements and with neutron diffraction results.

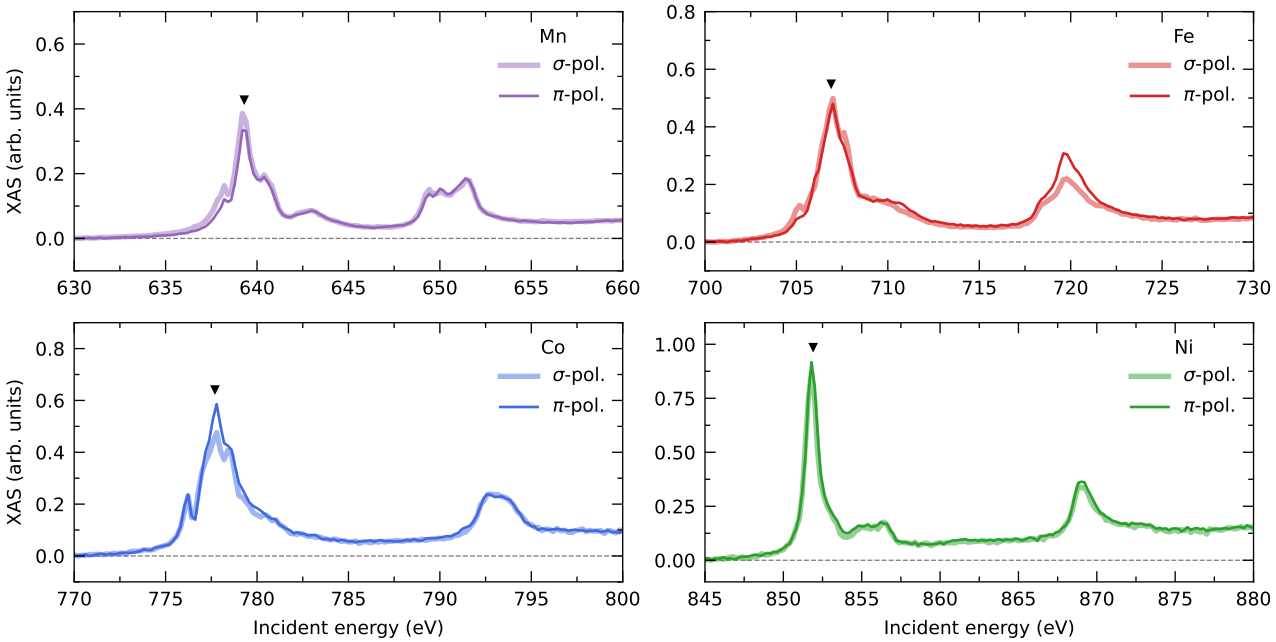

FIG. S11. **X-ray absorption spectrum (XAS) at the TM L edge measured at REIXS beamline for various elements and photon polarizations.** All measurements were performed in total fluorescence yield (TFY) mode at $\theta = 20°$ and $T = 21$ K. The black triangles mark the photon energies at which **Q** scans were conducted in Fig. S12 and Fig. 3b–f of the main text. These patterns are consistent with previously reported XAS results for divalent transition metals.

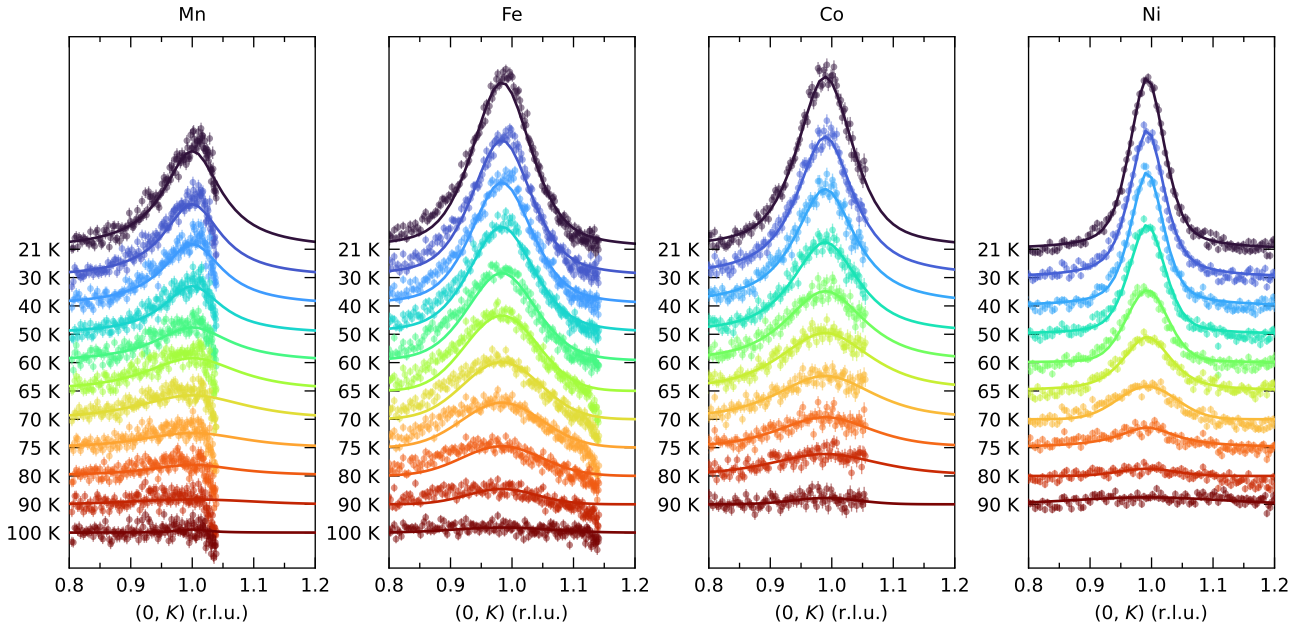

FIG. S12. **Background subtracted RSXS scans across the 2D magnetic signals at the indicated temperatures for different elements.** The solid lines are fitting results using pseudo-Voigt profiles. Note that the accessible **Q** range is limited, as the photons are blocked by the sample at large **Q**. The fitted peak heights are summarized in Fig. 3f of the main text.

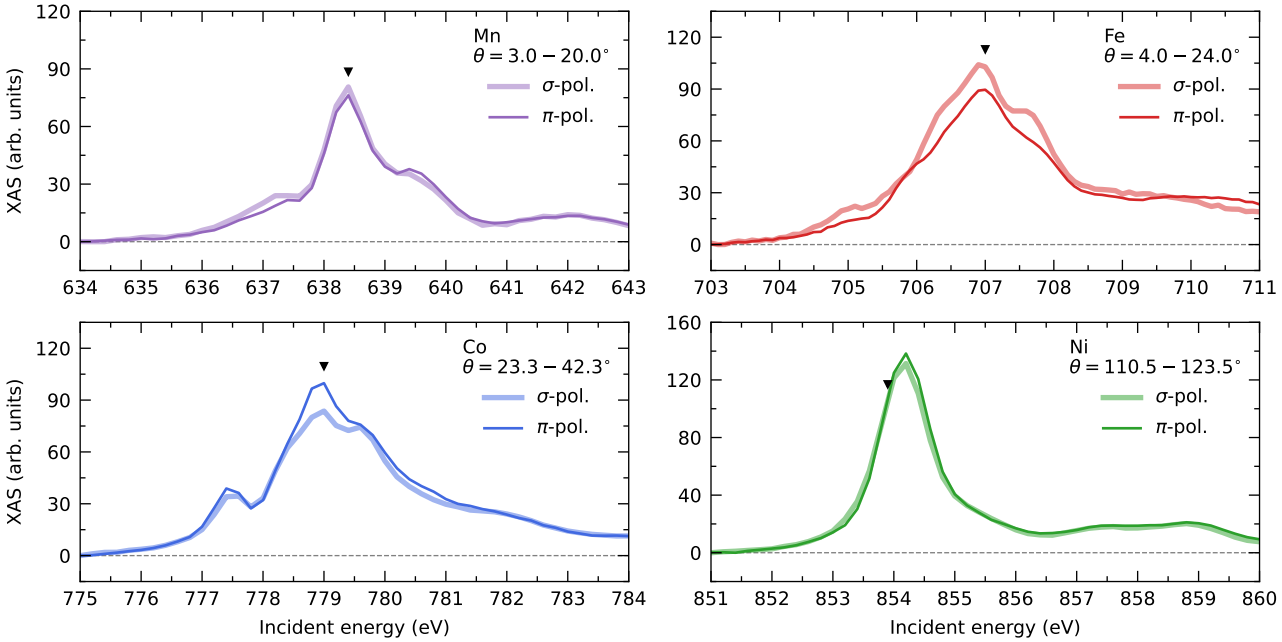

FIG. S13. **XAS measured at 13-3 beamline.** The data were collected using a two-dimensional (2D) detector with a rotation of the sample. Thus, counts from a range of θ are summarized, which are indicated in the plots. The black triangles indicate the photon energies where the RSXS scans were taken in Fig. 4 of the main text. The features are overall consistent with the REIXS results.

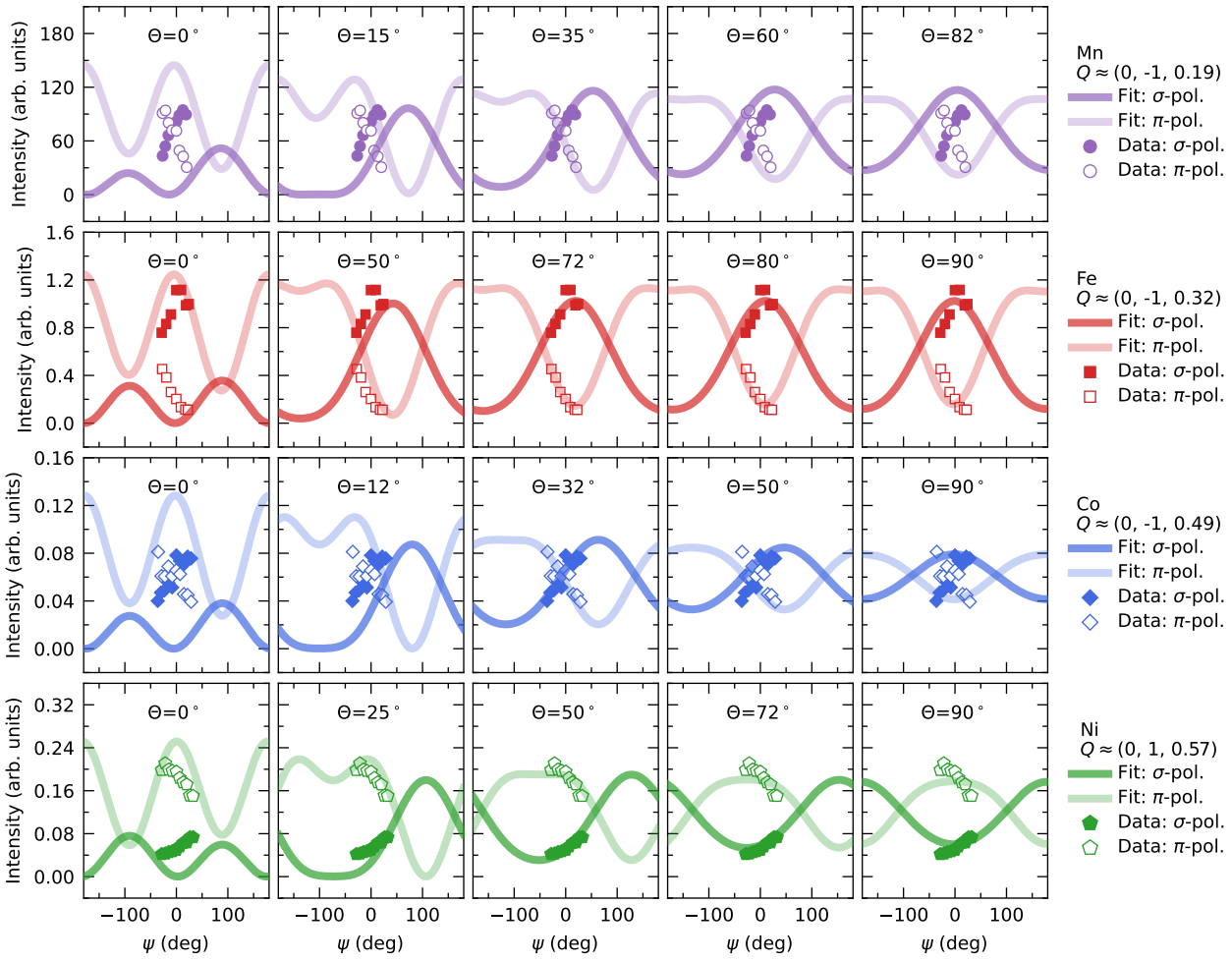

FIG. S14. **Azimuthal dependence of the magnetic signals calculated in the full range with different spin canting angles.** Note that the data at the Ni L edge were collected at positive K while others were measured at negative K due to background considerations. Additionally, ψ for $\mathbf{Q}$ with positive K corresponds to $\psi + 180°$ for symmetric $\mathbf{Q}$ with negative K.

[1] S. K. Choi, R. Coldea, A. N. Kolmogorov, T. Lancaster, I. I. Mazin, S. J. Blundell, P. G. Radaelli, Y. Singh, P. Gegenwart, K. R. Choi, S. W. Cheong, P. J. Baker, C. Stock, and J. Taylor, Spin waves and revised crystal structure of honeycomb iridate Na_2IrO_3, Physical Review Letters **108**, 127204 (2012).

[2] D. Lançon, H. C. Walker, E. Ressouche, B. Ouladdiaf, K. C. Rule, G. J. McIntyre, T. J. Hicks, H. M. Rønnow, and A. R. Wildes, Magnetic structure and magnon dynamics of the quasi-two-dimensional antiferromagnet $FePS_3$, Physical Review B **94**, 214407 (2016).

[3] J. Rodríguez-Carvajal, Recent advances in magnetic structure determination by neutron powder diffraction, Physica B: Condensed Matter **192**, 55 (1993).

[4] K. I. Kugel, D. I. Khomskii, A. O. Sboychakov, and S. V. Streltsov, Spin-orbital interaction for face-sharing octahedra: Realization of a highly symmetric SU(4) model, Physical Review B **91**, 155125 (2015).

[5] J. A. Sears, L. E. Chern, S. Kim, P. J. Bereciartua, S. Francoual, Y. B. Kim, and Y.-J. Kim, Ferromagnetic {Kitaev} interaction and the origin of large magnetic anisotropy in α-$RuCl_3$, Nature Physics **16**, 837 (2020).